

Supporting Information

Spectral characterization of mid-infrared Bloch Surface Waves excited on a truncated 1D photonic crystal

A. Occhicone^{1,‡}, M. Pea^{2,‡}, R. Polito^{3,‡}, V. Giliberti⁴, A. Sinibaldi¹, F. Mattioli², S. Cibella², A. Notargiacomo²,
A. Nucara³, P. Biagioni⁵, F. Michelotti¹, M. Ortolani^{3,4} and L. Baldassarre^{3,*}

¹ SAPIENZA University of Rome, Department of Basic and Applied Sciences for Engineering, Via A. Scarpa, 16, 00161 Roma, Italy.

² CNR-IFN, Consiglio Nazionale delle Ricerche, Institute for Photonics and Nanotechnologies, Via Cineto Romano, 42, 00156 Roma, Italy.

³ SAPIENZA University of Rome, Department of Physics, Piazzale Aldo Moro, 5, 00185 Roma, Italy.

⁴ Istituto Italiano di Tecnologia, Center for Life Nanosciences, Viale Regina Elena, 291, 00161 Roma, Italy.

⁵ Politecnico di Milano, Department of Physics, Piazza Leonardo da Vinci, 32, 20133 Milano, Italy.

* Corresponding author: leonetta.baldassarre@uniroma1.it

■ MATERIALS CHARACTERIZATION

Deposited layers surface characterization

The deposited single layers and multilayered structures (ML) have been characterized by atomic force microscopy (AFM). Films with different thickness have been deposited to follow the morphology evolution through the whole deposition process. Figure S.1a, b and c show AFM images of CaF₂ layers with increasing thickness (110, 1850 and 2750 nm respectively) evaporated on CaF₂ substrates. Initially, the CaF₂ layer is homogenous with a grainy like structure of the surface. Increasing the thickness, regular protruding structures emerge: panels S.1b (thickness of 1850 nm shown in plan view) and S.1c (thickness of 2750 nm shown with 3D rendering) show clearly a columnar triangular arrangement, as mentioned in the main text. On the other hand, the ZnS layers deposited on the CaF₂ substrates, with the CaF₂ adhesion layer, maintain a flat and homogeneous surface even for large thickness, as shown in Figure S.1d and e, were AFM images of 110 and 870 nm thick ZnS layers are reported. Figure S.1f reports the surface morphology of the multilayer with structure from top to bottom ZnS(50nm)/ CaF₂(2500nm)/ ZnS(200nm)/ CaF₂(2500nm)/ ZnS(200nm)/ CaF₂(adlayer)/ CaF₂ substrate) (structure B) and the corresponding FIB-SEM section is in the inset (note that the AFM image is shown in 3D rendering). Apparently, the triangular columnar structures, distinctive of the CaF₂ layers, are still quite well visible in the multilayered structures, pointing to a conformal coverage of the CaF₂ structures, confirmed

also by the FIB-SEM analysis (see Figure S.1g). This indicates that the intercalation of the ZnS layers between CaF₂ layers do not influence consistently the sample morphology, besides a granular fine structure of the surface essentially due to the presence of the 50 nm thick ZnS cap layer.

The surface morphology evolution can be quantitatively described in terms of the RMS surface roughness analysis, as shown in Figure S.2. It is apparent that upon increasing the thickness the roughness of the deposited CaF₂ (black square dots) increases up to a saturation value of about 30 nm. Conversely, the roughness of the deposited ZnS layers (red circle dots) decreases from an initial value of about 3 nm to values between 1-2 nm.

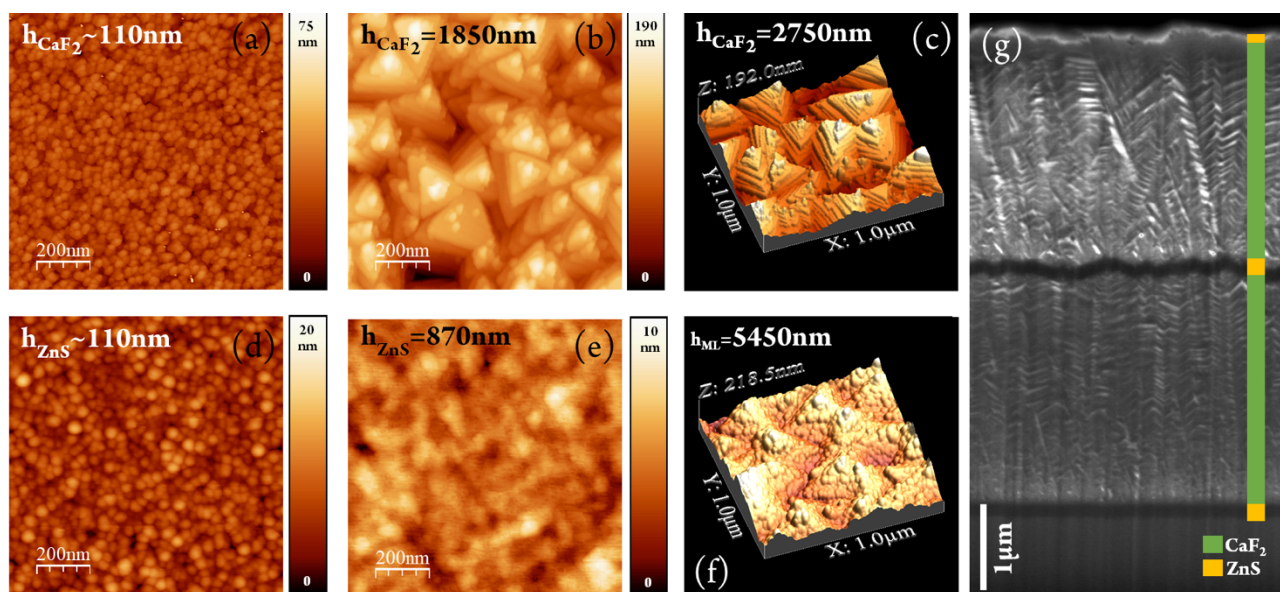


Figure S.1. AFM images (1×1 μm) of deposited layers: CaF₂ layers with thickness of (a) 110 nm, (b) 1850 nm, and (c) 2750 nm (in 3D rendering); ZnS layer with thickness of (d) 110 nm and (e) 875 nm; (f) multi-layered structure B in 3D rendering; (g) FIB-SEM cross sectional image.

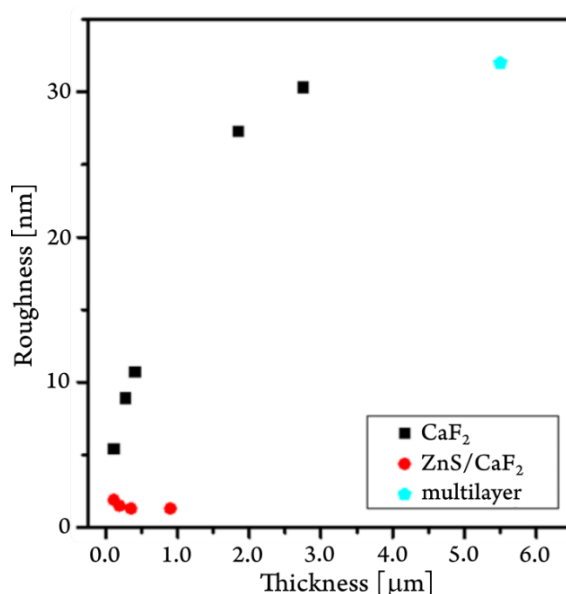


Figure S.2. Surface roughness of deposited CaF₂ (black square dots), ZnS (red circle dots) and of the multilayered structure B reported (pentagonal light blue dot).

In the same graph, the roughness of the multilayered structure B, described in Figure S.1, is reported (pentagonal light blue dot). This roughness value is compatible with the saturating behaviour of the CaF_2 roughness since, as previously pointed out, the deposition of the ZnS layers is essentially conformal.

Voids in the CaF_2 thick layers

The Figure S.3 shows a more magnified image of the upper part of the target multilayer shown in Figure 2 in the main text. The last 3 deposited layers are visible: ZnS top layer, CaF_2 and ZnS layers. The image permits to highlight the layers morphological properties described in the main text: the conformal deposition of the ZnS top layer and the presence of voids in the CaF_2 .

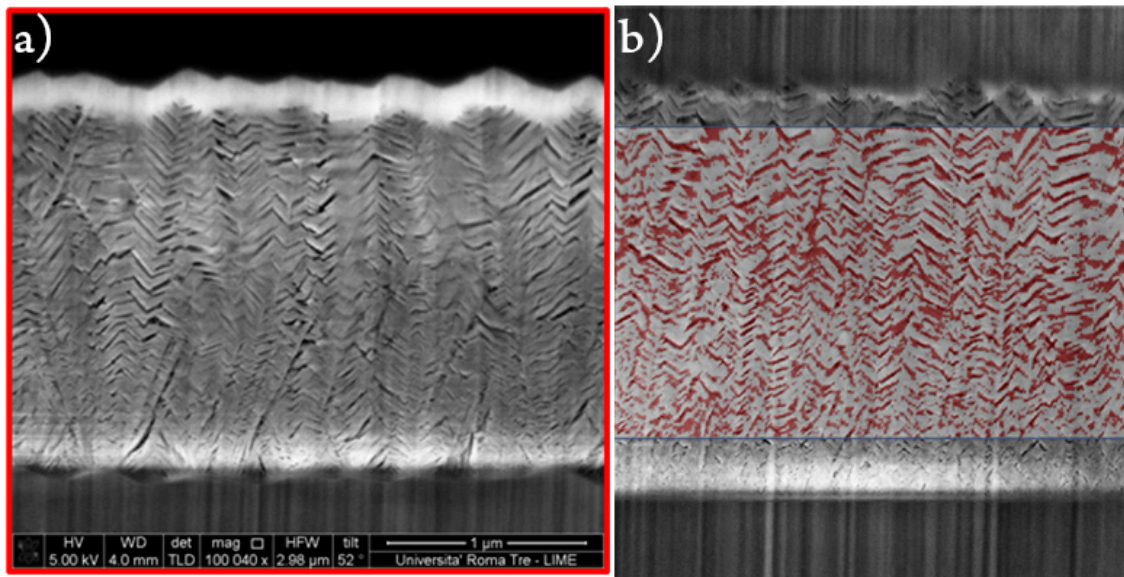


Figure S.3. a) Higher magnification image of the multilayered structure shown in the main text: ZnS top layer, CaF_2 and ZnS layers are visible. b) FIB/SEM cross section image of the lower layers in the multilayered structure described in the main text with superimposed void analysis layer (red/grey frame).

The FIB-SEM cross section morphological analysis permit to obtain an estimation of the void percentage in the CaF_2 layers. The images have been processed using the Image J analysis software. Wide enough FIB-SEM images were considered so that the extrapolated value can be representative of the whole sample and the images has been resized in order to account for the sample tilt angle. The Figure S.3b shows an example of the void analysis layer (red/grey frame) superimposed to a FIB-SEM cross section image (in grey scales), with red areas corresponding to the voids.

The area of the voids estimated by this procedure is around 30% of the total area, for both the CaF_2 layers in the multi-layered structure. Assuming that the voids visible on the surface section are homogeneously distributed in the volume, we can describe the film as an effective medium made by CaF_2 with 30% of voids [1]. This value is quite comparable with that found by fitting the infrared data, though somewhat lower. The discrepancy can be attributed to a partial filling of the voids' cavity due to the redeposition of FIB milled material during the definition of the cross section.

Infrared characterization of the deposited material

In order to assess the quality of the deposited materials, we have measured single layers of ZnS and CaF₂ as well as multilayers deposited on flat substrates. Transmission (Reflection) measurements have been performed at (near-) normal incidence. We find that there are small amounts of impurities that are incorporated in the CaF₂ layers, yielding some absorption peaks between 1000 and 2000 cm⁻¹ and at about 3000 cm⁻¹, while no evidence of absorption peaks is found for ZnS layers, as shown in Figure S.4a and b. We have performed a multi-Lorentzian fitting of the CaF₂ monolayer transmittance in order to extract the extinction coefficient (see Inset Figure S.4a), showing that, although present, these peaks are not intense.

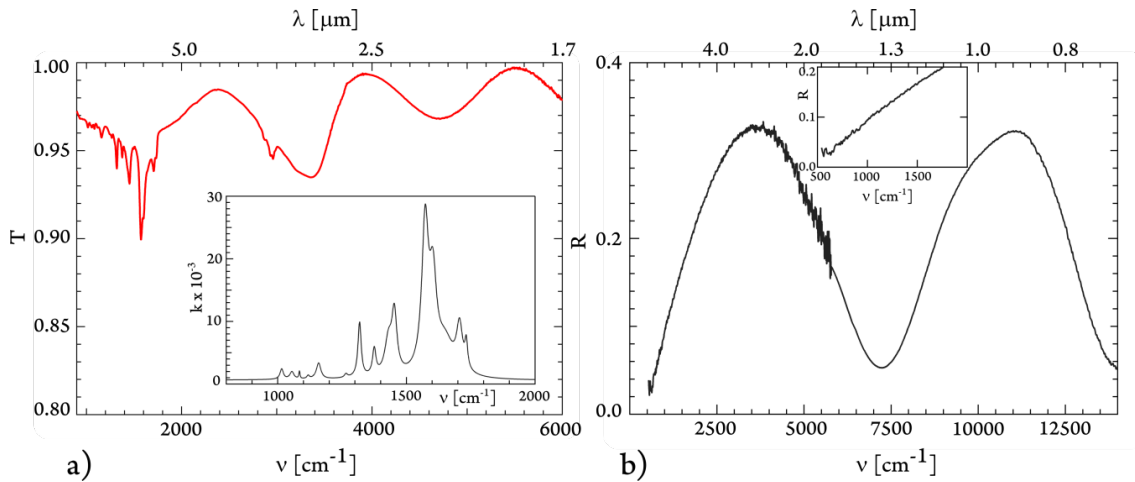


Figure S.4. a) Transmission spectrum of CaF₂ monolayer deposited on flat substrate. The inset shows the extinction coefficient (k) of impurities embedded in the CaF₂ evaporated layer obtained by multi-Lorentzian fitting. b) Reflection spectrum of ZnS monolayer deposited on flat substrate. The inset is a higher magnification of the range 500-2000 cm⁻¹.

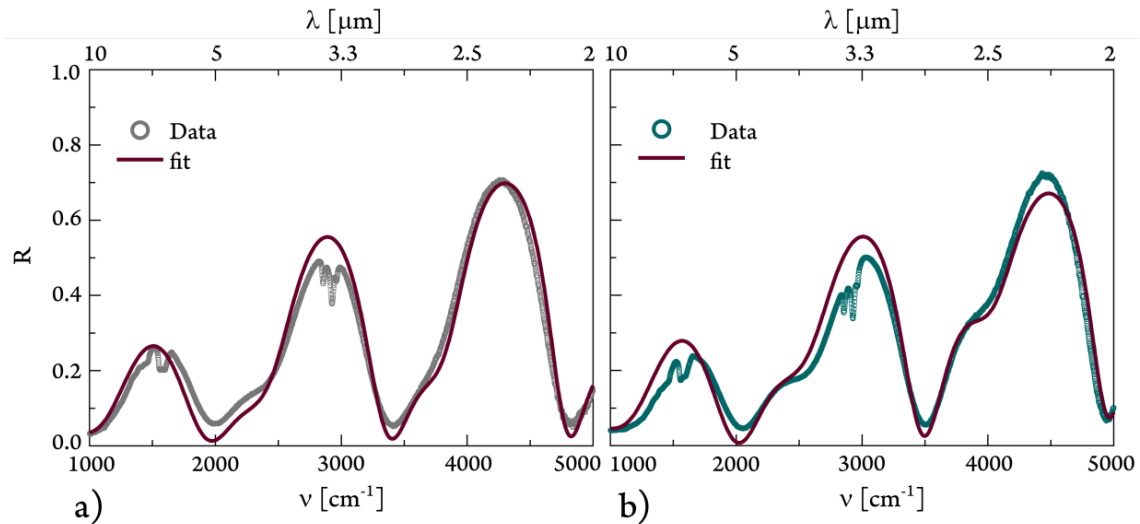


Figure S.5. Reflection spectra of the structures C and D in a) (grey dot curve) and in b) (green dot curve) compared with the corresponding fitting curve (bordeaux solid curve) obtained with a simplified Fresnel multilayer model.

We have moreover characterized several different multilayers, and for all of them we have performed fitting based on a simplified Fresnel multilayer model, neglecting losses and assuming all interfaces perfectly flat. We have taken as fixed thicknesses those obtained by

FIB-SEM cross sections, not taking into account the angle of incidence. The layers thicknesses sequence measured by FIB-SEM analysis are from top to bottom for C (D): ZnS 50nm (50 nm)/ CaF₂ 2600nm (2430 nm)/ ZnS 215nm (190)/ CaF₂ 2600nm (2500)/ ZnS 180nm (215)/ CaF₂(adlayer)/ CaF₂ substrate. In the Figure S.5a and b, we show reflection measurements performed at (near-) normal incidence of the multilayers structure C and D compared with the corresponding fit curves. We get refractive index values of $n = 1.20 \pm 0.05$ and 2.20 ± 0.02 for CaF₂ and ZnS, respectively, as for the multilayered structure described in the main text confirming that the layers morphological properties described above are highly reproducible.

■ NUMERICAL METHODS

Transfer Matrix Method

The distribution of the electric field inside each homogeneous layer can be expressed as the sum of an incident plane wave and a reflected plane wave. The complex amplitudes of these waves are the elements of a column vector [2]. The electric field into the external medium in contact with the dielectric stack (1DPC) is related to the field into the incidence medium by the following:

$$\begin{pmatrix} a_0 \\ b_0 \end{pmatrix} = \mathbf{M} \begin{pmatrix} a_{N+1} \\ b_{N+1} \end{pmatrix}$$

where \mathbf{M} is the multilayer transfer matrix:

$$\mathbf{M} = \left(\prod_{k=1}^N \mathbf{R}_{k-1,k} \mathbf{T}_k \right) \mathbf{M}_{N,N+1}$$

with:

$$\mathbf{R}_{p,q} = \frac{1}{t_{pq}} \begin{pmatrix} 1 & r_{pq} \\ r_{pq} & 1 \end{pmatrix} \quad \text{Interface Matrix}$$

$$\mathbf{T}_q = \begin{pmatrix} e^{jk_q d_q} & 0 \\ 0 & e^{-jk_q d_q} \end{pmatrix} \quad \text{Propagation Matrix}$$

r_{pq} is the Fresnel reflection coefficient calculated at the interface between the layers p and q and it depends on the electromagnetic wave polarization (σ , π or their combination), the incident angle and the materials' refractive index. The coefficient t_{pq} is equal to $1 + r_{pq}$. d_q is the layer thickness where the electromagnetic wave is propagating. k_q is the component of the wavevector perpendicular to the interface and is equal to $\sqrt{\left(\tilde{n}_q \frac{\omega}{c}\right)^2 - \beta^2}$, where $\tilde{n}_q = n_q + j\kappa$ is the complex refractive index of the material q , ω the angular frequency of the electromagnetic wave and c the speed of light in the vacuum.

The reflection coefficient (complex number) of the whole multilayer is calculated by the following:

$$r = \frac{m_{2,1}}{m_{1,1}}$$

where $m_{2,1}$ and $m_{1,1}$ are the elements of the matrix \mathbf{M} . The multilayer reflectance is obtained by the following:

$$R = |r|^2$$

1DPC Optimization procedure

To optimize the 1DPC structure to sustain a BSW in the Mid-IR wavelength range, we started from the material refractive index reported in literature. In particular, for the CaF₂ we used the following [3]:

$$n_{CaF_2} = \lambda \sqrt{1 + \frac{\lambda^2 a_1}{\lambda^2 - b_1} + \frac{\lambda^2 a_2}{\lambda^2 - b_2} + \frac{\lambda^2 a_3}{\lambda^2 - b_3}}$$

with:

$$a = (a_1, a_2, a_3) = (0.5675888, 0.4710914, 3.8484723)$$

$$b = (b_1, b_2, b_3) = (0.00252643, 0.01007833, 1200.555973)$$

For the ZnS, we used the following one [4]:

$$n_{ZnS} = \sqrt{g_1 + \frac{g_2}{\lambda^2 - e_1^2} + \frac{g_3}{\lambda^2 - e_2^2}}$$

with:

$$g = (g_1, g_2, g_3) = (8.393, 0.14383, 4430.99)$$

$$e = (e_1, e_2) = (0.05861241, 1347.6241)$$

For both the relations, λ is the radiation wavelength in μm .

As reported in the main text, the deposited materials are characterized by a porosity that is not neglectable. To take into account the porosity, we used the Maxwell – Garnett mixing rule [5] to calculate the refractive index of the composite material:

$$n_{MG}^2 = \varepsilon_{MG} = \varepsilon_0 \frac{2(1 - v_i)\varepsilon_0 + (1 + 2v_i)\varepsilon_i}{(2 + v_i)\varepsilon_0 + (1 - v_i)\varepsilon_i}$$

where v_i is the fraction volume of the inclusions, ε_i the dielectric constant of the included material and ε_0 the dielectric constant of the matrix material. We considered a fraction volume of the voids inclusion of about 40%.

A multilayer stack characterized by a periodical refractive index function shows the opening of photonic band gaps where the light cannot propagate, as extensively discussed in literature [6]. For two materials with refractive indices n_L and n_H and thicknesses d_L and $d_H = \Lambda - d_L$, where L and H stay for low and high refractive index, respectively, the normal-incidence photonic gap is maximized when [6]:

$$\frac{d_L}{\Lambda} = \frac{n_H}{n_L + n_H} \quad (\text{S. 1})$$

In this specific case, it can be demonstrated that the mid-gap wavelength in vacuum is [6]:

$$\lambda_m = \frac{4\Lambda n_L n_H}{n_L + n_H}$$

By using the relation $k_m = \frac{2\pi}{\lambda_m}$, we can obtain the following:

$$k_m = \frac{n_L + n_H}{4n_L n_H} \cdot \frac{2\pi}{\Lambda}$$

Taking into account the incident angle θ , we can write:

$$k_m = k_{\perp} = k \cos \theta = \frac{2\pi}{\lambda_0} \cos \theta = \frac{n_L + n_H}{4n_L n_H} \cdot \frac{2\pi}{\Lambda} \Rightarrow \Lambda = \frac{\lambda_0 (n_L + n_H)}{4n_L n_H \cos \theta} \quad (\text{S. 2})$$

By choosing $\lambda_0 = 5.6 \mu\text{m}$, as reported in the main text, and $\theta = 55 \text{ deg}$, equal to the basis angle of the CaF_2 truncated prism used for our experiments (see main text), we obtain $\Lambda = 3.1 \mu\text{m}$ and d_H/Λ ratio equal to about 0.65 (*quarter-wave stack*).

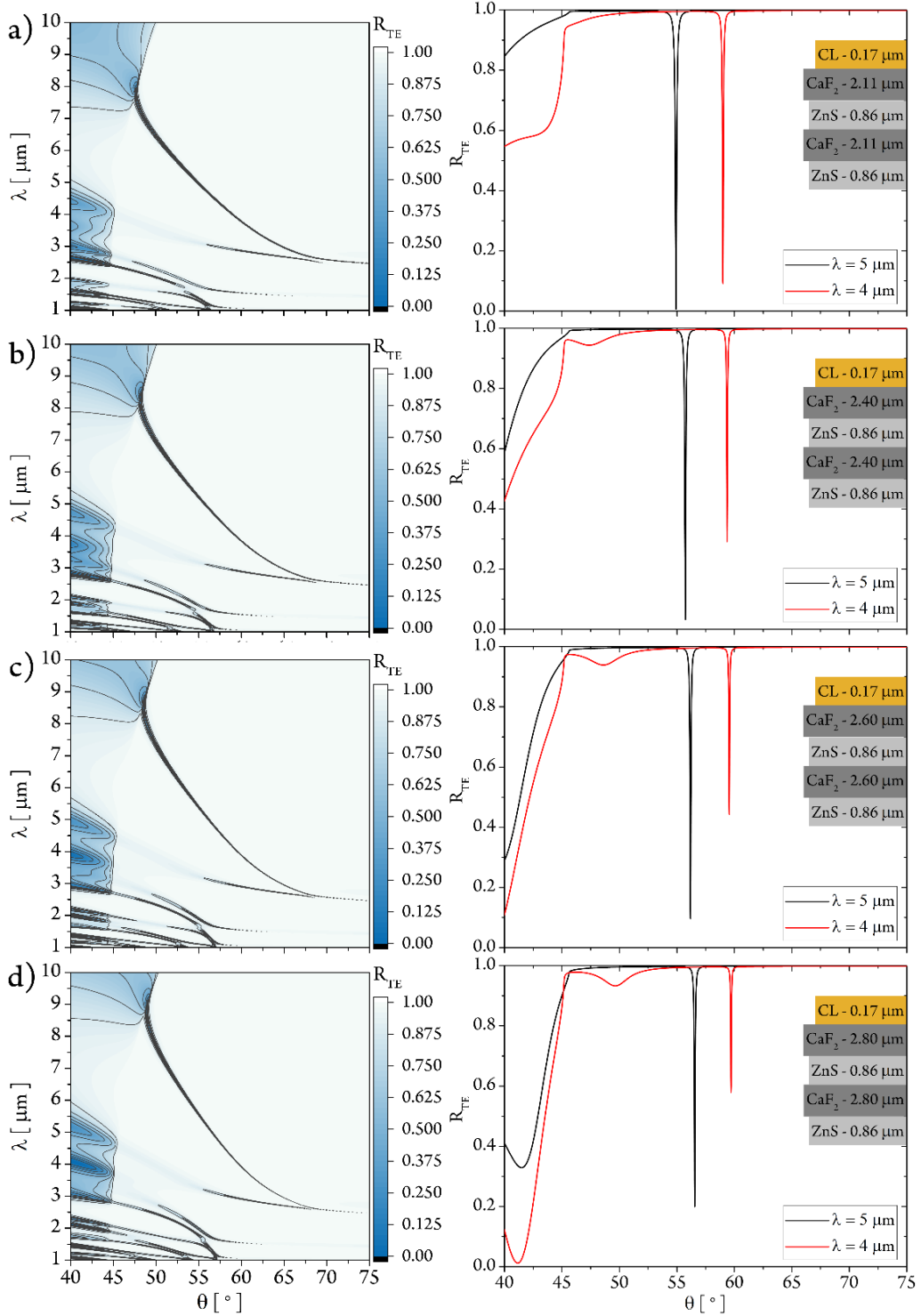


Figure S.6. Reflectance maps (left) and 2D reflectance profiles (right) calculated for different 1DPC structures. In the 2D plots, we plot the reflectance profiles obtained for $\lambda = 4 \mu\text{m}$ and $\lambda = 5 \mu\text{m}$. In the insets, we sketch the simulated structures obtained by increasing the low refractive index material thickness (going from a) to d)).

In Figure S.6., we report some examples about the reflectance map calculated for the structures sketched in the insets. To optimize the structure, we started from the values of d_L and d_H obtained through the Eqs. (S. 1) and (S. 2). For the sake of simplicity, we report only the reflectance maps obtained by changing the low refractive index layers thicknesses (CaF_2). The reflectance maps, as in the main text, are calculated for θ ranging from 40 to 75 deg, whereas the wavelength from 1 to 10 μm . From the reflectance map, we can retrieve information about the dependence of the BSW angular position on the wavelength. By increasing the CaF_2 thickness, the BSW dispersion shows a larger slope, thus indicating a larger sensitivity of the BSW angular position to wavelength changes. On the contrary, the 2D reflectance signal plotted by cutting the reflectance maps at $\lambda = 4 \mu\text{m}$ and $\lambda = 5 \mu\text{m}$ shows that by increasing the low refractive index layer thickness (going from the figure a) to d)) the BSW resonance appears less deep. Moreover, the BSW dip moves to higher angles, far from $\theta = 55$ deg. By further increasing the thickness of the low refractive index layers, the BSW resonance disappears in the range of angles and wavelength used in our experiments. Similar results are obtained by changing the high refractive index layer thickness. By fixing $d_L = 2.20 \mu\text{m}$, for d_H larger than $1.1 \mu\text{m}$, the BSW resonance dip disappears from the angular and spectral range of our interest.

In Figure S.7., we report the optimal structure: $d_L = 2.20 \mu\text{m}$ and $d_H = 1.00 \mu\text{m}$. The BSW resonance appears deeper because of the maximum field enhancement (see main text). By properly fixing the cap layer thickness to $d_{CL} = 200 \text{ nm}$, the BSW angular position is located at $\theta = 55.2$ deg at λ_0 . A larger cap layer thickness means a larger BSW angular position.

In conclusion, by taking into account the accuracy of the deposition technique, the structure we proposed is $d_L = 2.25 (\pm 0.15) \mu\text{m}$, $d_H = 0.95 (\pm 0.10) \mu\text{m}$ and $d_{CL} = 0.19 (\pm 0.04) \mu\text{m}$, as reported in the main text.

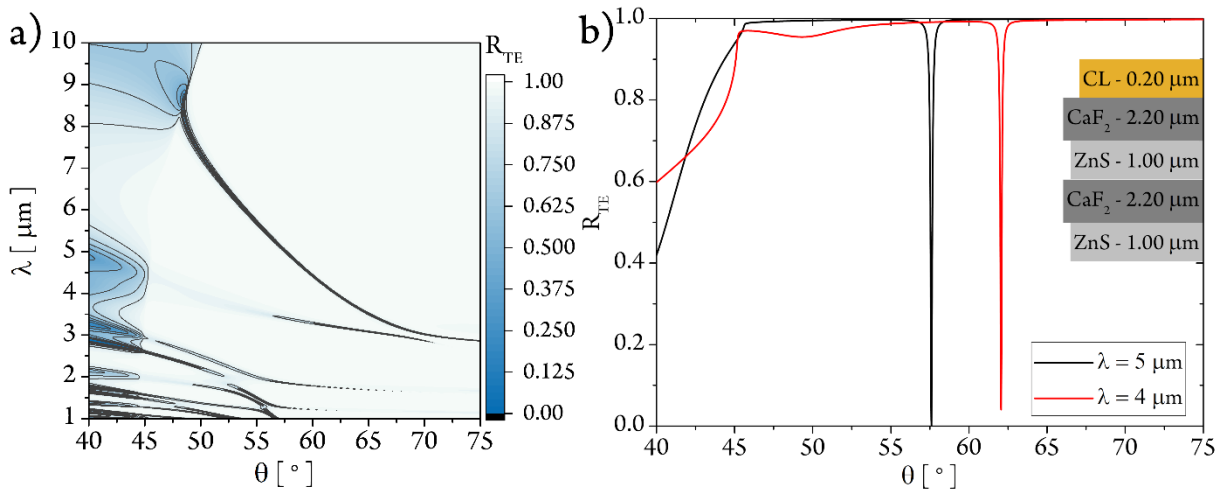


Figure S.7. a) Reflectance map calculated for the optimized 1DPC. b) Reflectance profiles obtained for $\lambda = 4 \mu\text{m}$ and $\lambda = 5 \mu\text{m}$.

FoM calculation

To calculate the propagation and the confinement FoM of the 1DPC reported in the main text, we used the propagation and the confinement distances reported in Figure S.8. The BSW propagation distance (l_m), is obtained by using the Eq. (2) in the main text and it is obtained from the Eq. (59) in the ref. [7]:

$$l_m = (kK)^{-1}$$

where:

$$k = \frac{2\pi}{\lambda}$$

and

$$K = \frac{\partial \xi}{\partial \theta} \Delta \theta = n_p \cos \theta \Delta \theta$$

with $\xi = n_p \sin \theta$, θ is the incidence angle and n_p is the prism refractive index.

On the contrary, the surface electromagnetic penetration depth (l_d) is evaluated by the following:

$$l_d = \frac{1}{2k_x} = \frac{\lambda}{4\pi \sqrt{n_p^2 \sin^2 \theta_{BSW} - 1}}$$

where k_x is the wavevector component perpendicular to the multilayer interfaces, and θ_{BSW} the BSW resonance angle.

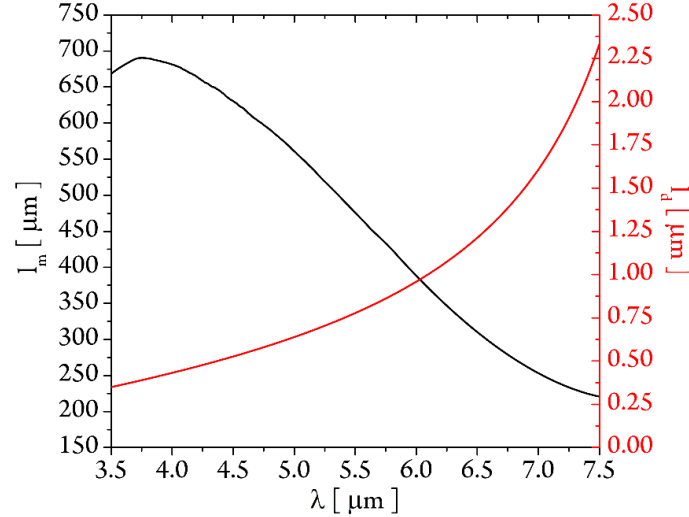


Figure S.8. Propagation (black) and confinement (red) distances plot as a function of the wavelength.

To evaluate the BSW propagation distance by the Eq. (2) and the penetration depth, we found the formula parameters from the reflectance map calculated by TMM and reported in Figure 5(a) in the main text. For each wavelength ranging from 3.5 to 7.5 μm , the BSW resonance dip has been fitted by a Lorentzian curve:

$$R_\lambda(\theta) = R_0 + \frac{2A}{\pi} \cdot \frac{\Delta \theta}{4(\theta - \theta_{BSW})^2 + \Delta \theta^2}$$

The fitting procedure provides the dip central angle ($\theta_{BSW}(\lambda)$) and the dip full width half maximum (FWHM, $\Delta\theta(\lambda)$).

As an alternative method to evaluate the FoMs, we have resorted to a second possible way to calculate the propagation lengths starting from the definition of quality factor as the ratio between the energy (E) stored in the oscillating resonator and the energy dissipated per cycle by damping processes (ΔE). Therefore, we can write $Q = \frac{\omega_0}{\Delta\omega} = 2\pi \frac{E}{\Delta E} = \frac{\theta_0}{\Delta\theta}$ where θ_0 is the incidence angle and $\Delta\theta$ the full-width half maximum. The propagation length is then evaluated as $l_{FWHM} = \tau c = \frac{Q\lambda_0}{\pi}$ where $\tau = \frac{2Q}{\omega_0}$ is the time in which energy is reduced by a factor $\frac{1}{e}$.

We have evaluated the propagation length of an SPP excited in the Kretschmann-Raether configuration in an 80 nm thick gold (Au) film. By choosing $\theta_0 \cong 43.5^\circ$ and $\Delta\theta \cong 0.7^\circ$ one obtains $l_{FWHM} \cong 12.5 \mu\text{m}$ that is close to $l_{th} = \frac{1}{2\text{Im}(k_x)} \cong 10 \mu\text{m}$, where $\text{Im}(k_x) \cong$

$$\sqrt{\frac{\epsilon'_{Au}}{1+\epsilon'_{Au}} \frac{\epsilon''_{Au}}{2\epsilon''_{Au}(1+\epsilon'_{Au})} \frac{\omega}{c}} \text{ and } \epsilon_{Au}(\lambda_0 = 633 \text{ nm}) \cong -11.75 + i1.25.$$

By following the same line of thought, we can estimate the propagation length in this way for the BSW, by considering wavelength and FWHM from our simulations. The results show that l_{FWHM} is larger than what discussed in the paper, yielding higher values of FoM_{prop} , that are however still lower than those of Au at infrared wavelengths. We report in Figure S.9 the comparison among the propagation lengths calculated as reported in the main paper and with this approximation.

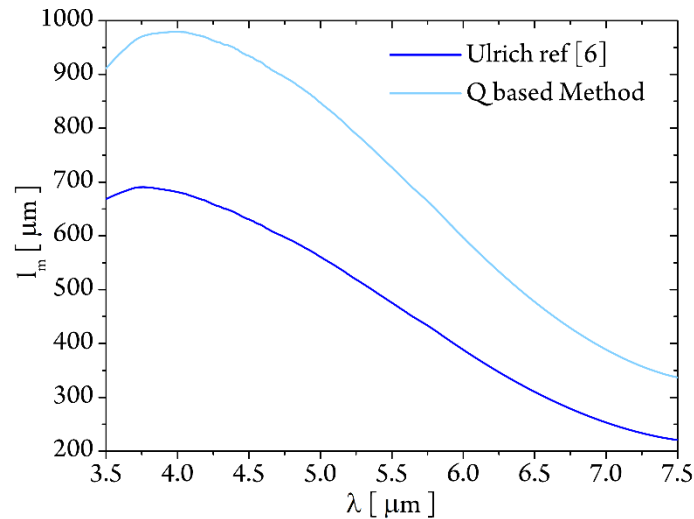


Figure S.9. Comparison of the propagation length, plotted with respect to the wavelength, calculated either as described in the main paper [7] (dark blue) or with the method described above (light blue).

■ REFERENCES

- [1] S. Giordano, "Effective medium theory for dispersions of dielectric ellipsoids," *J. Electrostatics*, vol. 58, no. 1–2, pp. 59–76, 2003.

- [2] P. Yeh, A. Yariv, and C.S. Hong, "Electromagnetic propagation in periodic stratified media. I. General theory," *J. Opt. Soc. Am.*, vol. 67, pp. 423-438, 1977.
- [3] I.H. Malitson, "A Redetermination of Some Optical Properties of Calcium Fluoride," *Appl. Opt.*, vol. 2, no. 11, pp. 1103-1107, 1963.
- [4] M. Debenham, "Refractive indices of zinc sulfide in the 0.405-13- μ m wavelength range," *Appl. Opt.*, vol. 23, no. 14, pp. 2238-2239, 1984.
- [5] R.W. Cohen, G.D. Cody, M.D. Coutts, and B. Abeles, "Optical Properties of Granular Silver and Gold Films," *Phys. Rev. B*, vol. 8, p. 3689, 1973.
- [6] J. Joannopoulos, S.G. Johnson, J.N. Winn, and R.D. Meade, *Photonic Crystals*, Princeton: Princeton University Press, 2008.
- [7] R. Ulrich, "Theory of the Prism-Film Coupler by Plane-Wave Analysis," *J. Opt. Soc. Am.*, vol. 60, no. 10, pp. 1337-1350, 1970.